PCCP

Accepted Manuscript

ROYAL SOCIETY OF CHEMISTRY

www.rsc.org/pccp

Journal Name

RSCPublishing

ARTICLE

Stable Compositions and Structures in the Na-Bi System

Cite this: DOI: 10.1039/xoxxoooooox

Xiyue Cheng,[a] Ronghan Li[a], Dianzhong Li[a], Yiyi Li[a] and Xing-Qiu Chen[a]

Received ooth January 2012,
Accepted ooth January 2012

DOI: 10.1039/xoxxoooooox

www.rsc.org/

At P = 1 atm the only stable compounds in the Na-Bi binary system are Na_3Bi and NaBi, which have been recently discovered to exhibit intriguing electronic behaviour as a 3D topological Dirac semimetal and a topological metal, respectively. By means of the first-principles calculations coupled with the evolutionary structural searches, we have systematically investigated the phase stabilities, the crystal structures and the corresponding electronic properties of the binary Na-Bi system. At ambient pressure, our calculations have reproduced well the experimentally observed compositions and structures of Na_3Bi and NaBi. At high pressures, we have found that Na_3Bi transforms from the ground-state hexagonal *hP*24 phase to a cubic *cF*16 phase above 0.8 GPa, confirming previous experiments, and then to a conventional band insulating *oC*16 phase above 118 GPa. The cubic *cF*16 phase would exhibit novel topological band ordering similar to that in HgTe. The topological metal NaBi has also been found to undergo a structural phase transition from an ambient tetragonal *tP*2 to a cubic *cP*2 structure above 36 GPa. Four never-reported Na_6Bi, Na_4Bi, Na_2Bi and $NaBi_2$ compounds with new compositions have been predicted to be experimentally synthesizable over a wide range of pressures starting at 142.5 GPa, 105 GPa, 38 GPa and 171 GPa, respectively. Moreover, a common charge transfer from Na to Bi has been revealed for all compounds, but the large interstitial charge localizations in the Na atomic cages have been noticed only in two compounds of Na_6Bi and Na_4Bi, which may associate with the close-packed Na environments.

1. Introduction

The High-throughput (HT) computational materials design is an emerging and booming area of materials science, along with the rapid innovation on the supercomputers and the development of crystal structural prediction algorithms[1-4]. It is a direct and effective way toward the growing endless demand for materials, comparing with the relatively costly and time-consuming experimental synthesis procedures. The HT computational materials design is the art of the organic combination of i) creating large-scale foundation database of materials (known or predicted), such as crystal structure, thermodynamic data, electronic structure, ii) selecting materials based on the demanding properties (i. e. enthalpy, band gap, hardness, etc.), and iii) the high-capacity exchange, transmission and storage of database. This concept has been widely applied to the designing of a number of materials, for example, the superhard materials, topological insulators, light-absorbing materials, thermoelectric materials, catalysis, and so on[1-9].

In principle, no matter what kind of material from computational design, the most essential part is structure. The crystal structure decides the intrinsic property of one material. Therefore, the prediction and calculation of crystal structures can be seen as an effective way to design new materials. From literature, based on the theoretical crystallographic prediction algorithms[6], such as genetic algorithm, simulated annealing, topological modelling and molecular packing approaches, etc., several prediction codes were successfully developed, including USPEX[10, 11], AFLOW[12], AIRSS[13], MAISE[14], CALYPSO[15], G42[16] and KLMC[17] code. These methods make it possible to search stable compositions and simultaneously determine the corresponding crystal structures in multi-component systems which was deemed as an "impossible task" just 20 years ago[18]. At present, these effective computational crystal structure prediction tools in combination with the state-of-the-art *ab initio* applications based on the density functional theory (DFT) have become one of the essential parts of HT computational materials design[5-17, 19-33]. On the one hand, at ambient pressure, most of the researches related with crystal structure prediction focused on a series of borides, carbides, and nitrides[22, 34-40], especially for the discovery of superhard materials. On the other hand, for the high pressure researches, they were also greatly fostered by these crystallographic prediction methods[30, 31] in the fields of the new phases of pure elements (Li, Na, Ca, B, etc.[41-45]), earth and planetary materials ($MgSiO_3$, Mg-O,

H_2O, etc.[23, 25, 46-52]), new functional materials (superconductors[53-56], superhard materials[57, 58], hydrogen storage materials[59], etc.), and novel chemical reactions (Xe-O, Na-Cl, Cs-F, etc.[60-66]). For instance, the Na-Cl system with only one 1:1 compound (NaCl) at ambient pressure was predicted to have several new stable compounds with unusual compositions (Na_3Cl, $NaCl_3$, $NaCl_7$, etc.) at high pressures[61]. The predicted cubic and orthorhombic phases of $NaCl_3$ and the two-dimensional metallic tetragonal Na_3Cl have even been experimentally confirmed. Interestingly, the high pressure can also give rise to unique atomic electronic states and even alter the intrinsic character of the inner-shell electrons. Most recently, the alkali metal Cs, normally assumed expressing the 1+ oxidation state, has been predicted to exhibit a formal oxidation number n+ in CsF_n (n > 1) compounds under high pressure and the Cs constituent behaves chemically like a *p*-block element[60]. This fact suggests that the high pressure can blur the boundary of *s*- and *p*-block elements and active the inner-shell electrons. Therefore, the discovery of those rich and varied high pressure phases greatly enriches the understanding of material structure, chemical bonding and electronic properties.

Most recently, the only two known compounds in the Na-Bi binary system, Na_3Bi and NaBi, have attracted great interest as they were both demonstrated exhibiting unique and exciting electronic properties. In fact, this Na-Bi system stood out from ordinary intermetallic system right after one theoretical work predicting the Na_3Bi is a 3D topological Dirac semimetal (TDS)[67]. Subsequently, this fact has been experimentally confirmed[68, 69]. It has been evidenced that the TDS properties of Na_3Bi process unique electronic states. Namely, the conduction and valence bands touch only at the discrete Dirac points and disperse linearly in all directions in the Brillouin zone (BZ). Such distinct electronic structure of TDS makes Na_3Bi to be highly attractive due to its high electron mobility and conductivity in 3D materials as well as numerous quantum properties (e.g., the unique surface states in the form of Fermi arcs, the Weyl phases, the high temperature linear quantum magnetoresistance, the topological magnetic phases, and the quantum anomalous Hall effect[67-80]). Interestingly, as for the 1:1 compound of NaBi, it was theoretically demonstrated to be a native 3D topological metal[81] through the first-principles calculations, which exhibits the combined interesting properties of the electron-phonon induced superconductivity and the obviously anisotropic but extremely low lattice thermal conductivity. Without (with) the spin-orbit coupling (SOC) effect, the superconducting transition temperature T_C was derived to be 1.82-2.59 (2.92-3.75) K from the electron-phonon coupling strength λ = 0.71 (0.84) and the average velocity $\langle\omega_{\ln}\rangle$ = 40.8 (38.7) cm^{-1}), agreeing well with the experimental findings[82, 83]. In addition, by considering phonon vibrational eigenvalues in the whole BZ and the phonon relaxation time derived from the third-order force constants, it has been further revealed that NaBi exhibits an extremely low lattice thermal conductivity but an obviously anisotropic feature of $\kappa_\omega^{a\text{-}axis}$ = 3.98 $Wm^{-1}K^{-1}$along the *a*-axis and $\kappa_\omega^{c\text{-}axis}$ = 1.53 $Wm^{-1}K^{-1}$ along the *c*-axis at room temperature, respectively.

Apparently, those interesting and unique electronic properties of the two compounds at ambient pressure render the Na-Bi system attractive. Naturally, it would be desirable to know whether or not some other interesting compounds exist in this system. If looking back the history of the Na-Bi system, their structural phase transformations and the corresponding electronic states were not well studied, especially, under high pressures. Motivated by the previous successful researches on the diversity of phases and chemical reactions for several reported systems, we have decided to investigate the compositions and structures of the Na-Bi binary system, the corresponding electronic structures and bonding natures.

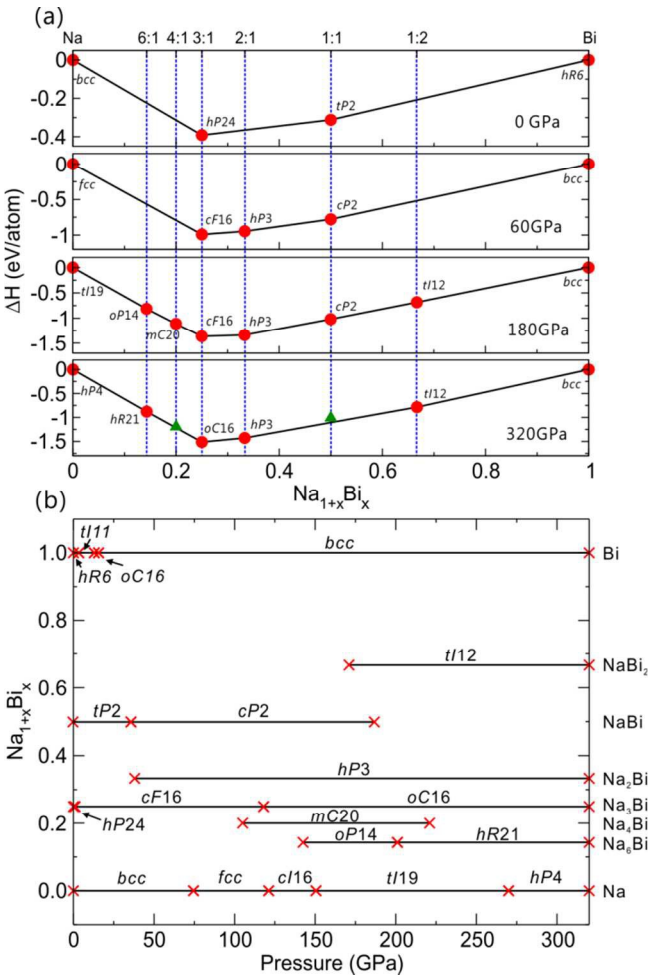

Figure 1. (Colour online) The stability of the Na-Bi compounds. (a) The enthalpies of formation Δ*H* (the convex hull diagrams) of $Na_{1-x}Bi_x$ under a range of pressures. The circles represent stable compounds, whereas the triangles denote thermodynamic metastable phases. (b) The predicted stable pressure ranges for $Na_{1-x}Bi_x$ compounds. The crosses indicate the pressure boundaries of the stability for each structure at one composition.

2. Computational Details

All the structural relaxations were performed within the framework of density functional theory (DFT)[84, 85] using the Vienna *ab initio* Simulation Package (VASP)[86, 87] with the projector augmented wave (PAW) method[88] and the

TABLE 1: The crystallographic details of structures of Na-Bi system. The calculated equilibrium lattice parameters, a (Å), b (Å, c (Å), and the optimized atomic sites of Na-Bi phases at given pressures (GPa).

Phases	Pearson Symbol	Space group	Pressure	Lattice Parameters	Atomic sites			
					Atom	x	y	z
Na	*cI*2	$Im\bar{3}m$	0	a = 4.174	Na	0	0	0
Na	*cF*4	$Fm\bar{3}m$	100	a = 3.504	Na	0.5	0.5	0.5
Na	*cI*16	$I\bar{4}3d$	120	a = 5.432	Na	0.044	0.044	0.044
Na	*tI*19	*I*4/*mcm* (host)	160	$a_H = a_G$ = 6.962	Na_H	0.7912	0.9126	0
		*C*4/*mmm* (guest)[a]		c_H = 3.477	Na_G	0	0	0
				c_G = 2.092				
Na	*oP*8	*Pnma*	160	a = 4.647	Na1	0.0182	0.25	0.1757
				b = 2.943	Na2	0.1605	0.25	0.5847
				c = 5.129				
Na	*hP*4	$P6_3/mmc$	280	a = 2.826	Na1	0	0	0.5
				c = 3.996	Na2	0.3333	0.6667	0.25
Bi	*hR*6	$R\bar{3}m$	0	a = 4.577	Bi	0	0	0.7653
				c = 11.999				
Bi	*mC*4	*C*2/*m*	3	a = 6.853	Bi	0.7507	0	0.1323
				b = 6.221				
				c = 3.267				
				β = 67.095°				
Bi	*tI*11	*I*4*mcm* (host)	7	$a_H = a_G$ = 8.564	Na_H	0.1506	0.6506	0
		*I*4/*mmm* (guest)[b]		c_H = 4.213	Na_G	0	0	0
				c_G = 3.165				
Bi	*oC*16	*Cmca*	14	a = 10.666	Na1	0.2843	0	0
				b = 6.339	Na2	0	0.1796	0.1781
				c = 6.356				
Bi	*cI*2	$Im\bar{3}m$	16	a = 3.729	Na	0	0	0
Na_3Bi	*hP*8	$P6_3/mmc$	0	a = 5.458	Na1	0	0	0.25
				c = 9.704	Na2	0.3333	0.6667	0.5827
					Bi	0.3333	0.6667	0.25
Na_3Bi	*hP*24	$P\bar{3}c1$	0	a = 9.458	Na1	0	0	0.25
				c = 9.674	Na2	0.3333	0.6667	0.2003
				a = 9.436[c]	Na3	0.3542	0.3187	0.0833
				c = 9.655[c]	Bi	0.3368	0	0.25
Na_3Bi	*cF*16	$Fm\bar{3}m$	1	a = 7.550	Na1	0.75	0.75	0.75
				a = 7.65[d]	Na2	0	0	0
					Bi	0.5	0.5	0.5
Na_3Bi	*oC*16	*Cmcm*	120	a = 3.852	Na1	0	0.6997	0.25
				b = 8.442	Na2	0	0.1114	0.0599
				c = 5.531	Bi	0	0.3999	0.25
NaBi	*tP*2	*P*4/*mmm*	0	a = 3.419	Na	0.5	0.5	0.5
				c = 4.890	Bi	0	0	0
				a = 3.46[e]				
				c = 4.80[e]				
NaBi	*cP*2	$Pm\bar{3}m$	40	a = 3.288	Na	0	0	0
					Bi	0.5	0.5	0.5
Na_2Bi	*hP*3	*P*6/*mmm*	40	a = 4.325	Na	0.3333	0.6667	0.5
				c = 3.004	Bi	0	0	0
Na_6Bi	*oP*14	*Pbam*	160	a = 4.003	Na1	0.0150	0.3371	0.2252
				b = 6.728	Na2	0.1590	0.1002	0.5
				c = 5.044	Bi	0	0	0
Na_6Bi	*hR*21	$R\bar{3}m$	240	a = 4.674	Na	0.5168	0.4832	0.0993
				c = 9.261	Bi	0	0	0
Na_4Bi	*mC*20	*C*2/*m*	160	a = 13.055	Na1	-0.8088	0	-0.4377
				b = 3.729	Na2	-0.8796	0	-0.2104
				c = 8.304	Na3	-0.1479	0	-0.2259
				β = 150.326°	Na4	-0.6624	0	-0.7157
					Bi	-0.5261	0	-0.8457
$NaBi_2$	*tI*12	*I*4/*mcm*	200	a = 5.788	Na	0	0	0.25
				c = 4.584	Bi	0.1588	0.6588	0

[a] Reference[89]. [b] Reference[90]. [c] Reference[91]. [d] Reference[92]. [e] Reference[93].

generalized gradient approximation (GGA) within the Perdew-Burke-Ernzerhof (PBE) exchange-correlation functional[94]. The adopted PAW-PBE pseudopotentials of Na and Bi treat $2p^6 3s^1$ and $5d^{10}6s^2 6p^3$ electrons as valences, respectively. The cutoff energy for the expansion of the wavefunction into plane waves was set at 350 eV. All the Brillouin zone integrations were

performed on the Monkhorst-Pack *k*-meshes and were sample with a resolution of $2\pi\times0.07$ Å^{-1}, which showed excellent convergence of the energy differences and stress tensors. For hexagonal structures, the Brillouin zone integrations were performed on the Γ-centered symmetry. Having identified the most stable compositions and structures, we relaxed them at pressures from 0 to 320 GPa with an even denser Monkhorst-Pack *k* -meshes with resolution $2\pi\times0.05$ Å^{-1}. The enthalpy, density of states and the band structures, either with or without the inclusion of spin-orbit coupling (SOC) of different phases was calculated using the Gaussian smearing method with the width of smearing in 0.01 eV, beside the semimetal Na_3Bi where the tetrahedron method with Blöchl corrections were utilized. The Bader charge analysis[95] and the electronic localized function (ELF)[96-98] was done using the grid-based algorithm with 100×100×100 grids.

To check the dynamical stability, we further derived the phonon dispersion curves using the finite-displacement approach as implemented in the *Phonopy* code[99]. The phonon frequencies are constructed from forces, resulting from displacements of certain atoms in a supercell containing typically 80-100 atoms for each $Na_{1-x}Bi_x$ compounds. In addition, all the crystal structure and the ELF diagrams, unless explicitly stated, were generated using VESTA[100].

Our predictions of stable phases with the lowest free energy were done using the USPEX code[10, 11] in the variable-composition mode which is capable to search the compositions and structures at same time.at 0 GPa, 60 GPa, 100 GPa, 180 GPa, 240 GPa, and 320 GPa. The code can actually compare the energy with different composition by itself via a global minimization of free-energy surfaces. The structures of the first generation were produced randomly and any combinations of numbers of atoms in the unit cell were allowed (within the total number $\leq$ 20). The new generations were created through heredity, random, lattice mutation and permutation of atoms, with probabilities of 60%, 10%, 20% and 10%, forming the structures pool after discarding 40% energetically worst structures. For each structure, five-step calculation in VASP with different precision is utilized in order to raise the searching speed. The population size was set to at least twice the number of atoms in the cell. We generally terminated the runs after 50 generations for each pressure. The convex hull for one system can be obtained directly after the variable-composition search. One can see the stable composition and a number of metastable structures clearly. We then rechecked the stable structures through VASP with very higher precision in order to obtain an accurate result. Meanwhile, the seed technique was applied during each structural search by adding the known structures from the experiments or previous searching results, in order to enhance the accuracy and efficiency of structural prediction. Finally, the obtaining stable structures were all recalculated using higher precision and denser *k*-meshes, especially for the Na and Bi elements which were used to obtain the formation energy.

It needs to be emphasized that before we started the extensive computations and analysis, we have compared the influence of different pseudo-potential (GGA and LDA) on the accuracy of the Na-Bi system. For instance, for the optimized lattice parameters for *hP*8-Na_3Bi, the LDA gives the estimated values of a =5.303 Å and c = 9.423 Å and the GGA yields a = 5.458 Å and c = 9.704 Å. It is clear that, in comparison with available experimental data (a = 5.448 Å and c = 9.655 Å) the lattice parameter obtained by GGA show a much better agreement with those LDA data. Thus, we believe that the GGA functional would be more suitable for the Na-Bi case. In particular, although the energy ranking may change because of the different pseudo-potential, we would give priority to more accurate calculation results. For this purpose, the GGA functional seems to be a better choice for the present system. In addition, it is well-know that the conventional DFT theory generally underestimate the band gap for some insulators and semiconductors. For instance, through conventional DFT calculation we ever estimated the occurrence of three-dimensional Dirac cone in Na3Bi[67] and this prediction was verified by experiments[68,69]. This fact demonstrated the reliability of our current DFT results. Therefore, we can trustily concluded that the inclusion of different types of exchange-correlation effects does not significantly alter our conclusion.

3. Computational Phase Diagram

Figure 1 summarizes the pressure-composition phase diagram of the binary Na-Bi system. The pressure-dependent enthalpies (ΔH) for $Na_{1-x}Bi_x$ have been obtained for the most stable structure as searched by USPEX. Here, the claim of the stability of a given compound is required to satisfy three prerequisites: (1) the negative formation enthalpy, (2) the thermodynamical stability in competing with its nearest neighboring two compositions, and (3) the dynamical stability via the phonon dispersions. Figure 1(a) compiles the convex hulls of the Na-Bi system at several selected pressures of 0 GPa, 60 GPa, 180 GPa and 320 GPa. The convex hull is defined as the line connecting the phases with the lowest formation enthalpies for all compositions discovered by USPEX and any compositions with the lowest-enthalpy structures lie exactly on the convex hull are deemed as the ground state phases in the Na-Bi system. Of course, the structures whose enthalpies stay above the convex hull would be thermodynamically metastable and, perhaps, can be synthesized under a peculiar situation. In this present paper, we only discuss the ground state phase for each composition at a certain pressure. In order to ensure the dynamical stability of one structure, we have performed the calculations of the phonon dispersions. If no imaginary phonon frequencies exist in the entire Brillouin zone, the structure can be thought to be dynamical stable. Note that the experimentally synthesized structures usually process the dynamic stability. However, it is not ensured that those synthesized phases are the real energetically ground-state phase as the thermodynamically metastable phase can be possibly synthesized.

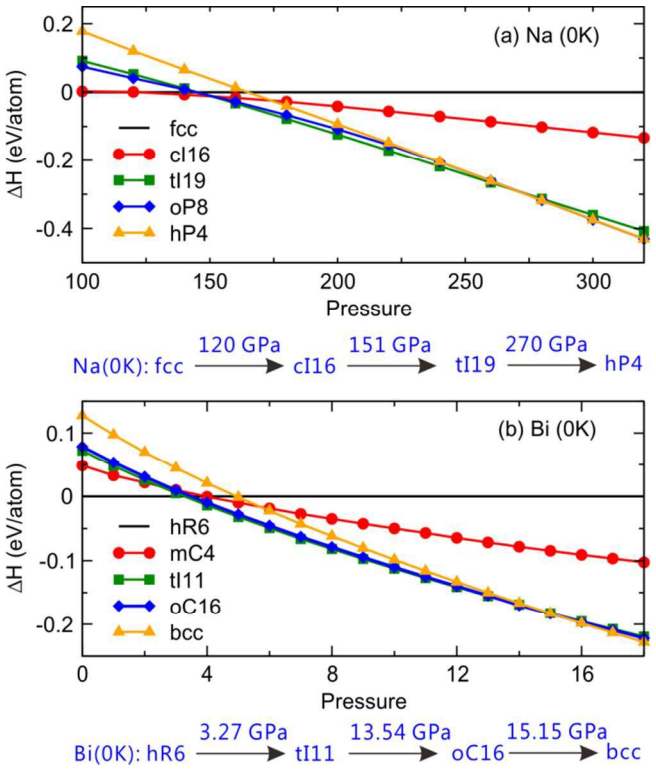

Figure 2. (Color online) The phase stability of Na and Bi. The relative enthalpy curves as a function of pressure at 0 K for (a) *cI*16, *tI*19, *oP*8, and *hP*4 structures of Na (relative to fcc), and (b) *mC*4, *tI*32, *oC*16 and bcc phases of Bi (relative to *hR*6). The insets show the transition sequences and pressures in more detail. It is noteworthy that temperature effects are not considered in the calculation, but might play an important structural role.

Furthermore, Fig. 1(b) illustrates the pressure-composition phase diagram. The black lines represent each composition and the crosses on the lines denote the pressure boundaries for the structural stability. Therefore, from Fig. 1(b) the stable pressure range for each structure of the discovered composition can be clearly visualized. In addition, we have also found that the vibrational entropic contribution, e.g., so-called zero-point energy (ZPE), only slightly affects the total energy and, typically, it did not change the relative stabilities by more than 10-15 meV/atom. The contribution of ZPE to the formation energy is thus small. Here, we neglect the ZPE contribution, when discussing the relative stability of the Na-Bi systems.

3.1 Stability of Na

For sodium, at ambient conditions it crystallizes in a body-centered cubic (bcc) structure and it transforms to a face-centered cubic (fcc) structure at around 65 GPa[101]. Then, a more complex body-centered cubic crystal structure containing 16 atoms in the unit cell (*cI*16) was experimentally observed at about 103 GPa[101, 102], and with further increasing the pressure, three transitions still occur[42, 43, 103-106]: an simple primitive orthorhombic structure with 8-atom unit cell (*oP*8) above 118 GPa, an incommensurate host-guest composite *tI*19 phase above 125 GPa and a double hexagonal close-packed structure *hP*4 around 200 GPa. The optimized lattice parameters and atomic sites of different Na structures at given pressures are listed in Table 1. Additionally, the stable pressure ranges and the enthalpy curves at high pressure of various Na phases are further illustrated in Fig. 1(b) and Fig. 2(a), respectively. From our currently first-principles calculations, it has been found that the *cF*16 phase is lower in energy than the fcc phase above the pressure around 120 GPa and the *oP*8 structure is less stable than the *tI*19 phase in the pressure range 148-270 GPa, but they are indeed energetically competitive (Fig. 2(a)). Moreover, the *oP*8 to *hP*4 phase transition was predicted at about 245 GPa and their continuous enthalpy curves show the nature of a second-order phase transition[43]. Finally, the *hP*4 structure becomes the stable phase at pressures above 270 GPa. For the incommensurate host-guest *tI*19 phase, it adopts a similar host tetragonal body-centered structure and atomic sites of K-III phase[89, 103]. The basic lattice parameters were taken from Gregoryanz *et. al*[103], where the host and guest tetragonal body-centered lattice parameters at 130 GPa are $a_H = a_G = 7.088$ Å , $c_H = 3.482$ Å and $c_G = 2.11$ Å . Of course, it is noteworthy that the temperature effects are not included in our present calculation but it might play an important role affecting the phase stability. It needs to be mentioned that our calculated enthalpy of Na phases are agree well with those from Ma *et. al*[43].

3.2 Stability of Bi

For bismuth, it crystallizes in a rhombohedral As-type structure with a six-atom unit cell (*hR*6) called Bi-I[107] at ambient condition. From our current calculations, the ground-state Bi-I phase can transform into an incommensurate composite host-guest structure *tI*11 (Bi-III) at 3.27 GPa (Fig. 1(b)). At 6.8 GPa, its experimental lattice parameters were reported to be $a_H = a_G = 8.518$ Å, $c_H = 4.164$ Å and $c_G = 3.180$ Å, giving a $c_H/c_G = 1.309$, with host and guest (space group *I*4*mcm* and *I*4/*mmm*) atoms at ($x = 0.1536$, $x + 0.5$, 0) and (0, 0, 0), respectively[90]. There are thus $8 + (2\times c_H/c_G) = 10.62$ atoms in the unit cell, but for simplicity, we prefer to call this Bi-III phase *tI*11. Then, at around 13.54 GPa, a 16-atom orthorhombic structure (called as Bi-IV[108]) is found to be less in energy than the *tI*11 phase. Afterwards, a bcc phase (called Bi-V) is calculated to be stable in a wide pressure region from 15.15 GPa to 320 GPa. In particular, the experimentally reported Bi-II phase, a 4-atom monoclinic structure (*mC*4), was measured to have a very narrow pressure range from 2.55 to 2.69 GPa at 298 K[107], but the *hR*6 to *mC*4 transition was reported to disappear at temperatures below 200 K and the *hR*6 phase transforms directly to the *tI*11 structure[109]. Indeed, our calculated enthalpy curve (Fig. 2(b)) demonstrates that this *mC*4 phase has a relatively higher energy as compared with the stability of either *hR*6 or *tI*11 phase at 0 K. This fact indicates its metastable nature at ground-state. In addition, the transition pressure for the *tI*11 and bcc-Bi was experimentally reported to be 2.7 GPa and 7.7 GPa at 298 K, respectively. However, our calculated transition pressures are relatively higher, which might associate with the unconsidered temperatures effects.

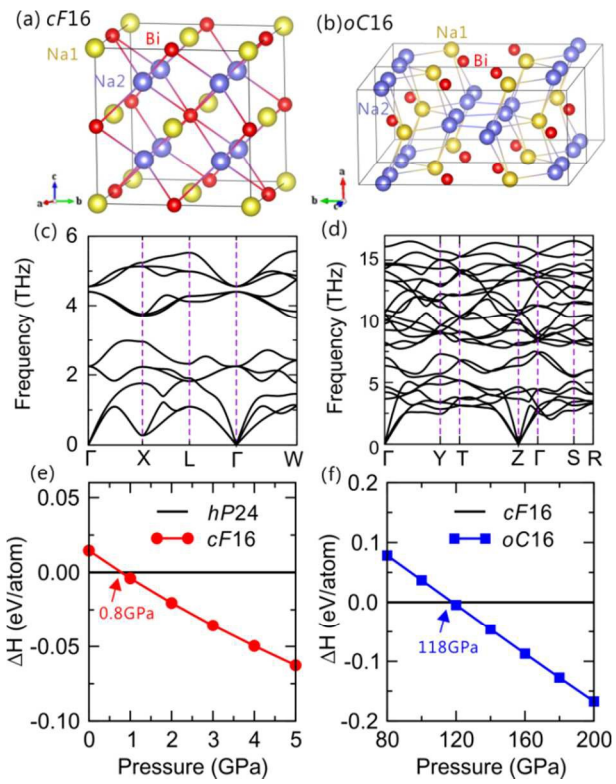

Figure 3. (Color online) The structural representations of (a) *cF*16 and (b) *oC*16-Na_3Bi at 1 GPa and 120 GPa, respectively. The corresponding phonon dispersion curves are shown in (c) and (d), respectively. (e) and (f) The relative energy as a function of pressure for *cF*16 and *oC*16-Na_3Bi, respectively. The structural transition pressure can be clearly seen for both phases.

3.3 Stability of compounds in the Na-Bi system

At ambient condition, our variable-composition computational searches have found two compounds of NaBi and Na_3Bi, in perfect agreement with the previous experiments and reported phase diagrams[110, 111]. To date, only these two compounds were synthesized in the Na-Bi system with the crystal structures of *tP*2 (space group $P4/mmm$)[93] and *hP*8 (space group: $P6_3/mmc$[112], respectively. Note that the ground state phase of Na_3Bi was experimentally suspected to be an *hP*24 (space group $P\bar{3}c1$) structure[91] and recently this fact has been confirmed theoretically[70].

As the pressure goes up, several never-reported compounds are predicted, as illustrated in Fig. 1. They are Na_2Bi, Na_6Bi, Na_4Bi, and $NaBi_2$ which are stable above 38 GPa, 105 GPa, 142.5 GPa, and 171 GPa, respectively. The most abundant compounds appear at around 180 GPa with six different compositions occur simultaneously. Moreover, from Fig. 1(b), several pressure-induced phase transformations can be seen, including *hP*24 to *cF*16-Na_3Bi at 0.8 GPa, *cF*16 to *oC*16-Na_3Bi at 118 GPa, *tP*2 to *cP*2-NaBi at 36 GPa, and *oP*14 to *hR*21-Na_6Bi at 201 GPa. Particularly, it needs to point out that our predicted transition pressure (0.8 GPa) of Na_3Bi from the ground state to the *cF*16 phase is in good agreement with the experimentally observed 0.7-1.0 GPa by Leonova *et al.*[92, 113] and Kulinich[114]. In addition, at pressures above 210 GPa, the *cP*2-NaBi is found no longer stable in the Na-Bi system and the *mC*20-Na_4Bi is also only stable at the pressure range of 105 to 201 GPa. Therefore, at 320 GPa, NaBi and Na_4Bi are denoted as thermodynamic metastable system, while the other four compounds (Na_6Bi, Na_3Bi, Na_2Bi and $NaBi_2$) remain as stable compositions.

4. Experimentally known phases

4.1. Na_3Bi

4.1.1. Structural stability and phonon dispersion

At ambient pressure, the early experimental measurements revealed that Na_3Bi crystallizes in the *hP*8 phase (space group $P6_3/mmc$, Na_3As-type structure). Our calculations demonstrated that this *hP*8 phase is dynamically unstable at the ground state due to the presence of large imaginary phonon frequencies around the *K* point[70]. Importantly, the *hP*24-Na_3Bi phase was suggested to be the real ground state and it was found obviously lower in energy than the *hP*8 phase and dynamically stable simultaneously[70]. The optimized crystal structural details for both the *hP*8 and *hP*24-Na_3Bi are listed in Table 1. It is highly attractive that this ground-state *hP*24-Na_3Bi is also a 3D topological Dirac semimetal, which can be deemed as a 3D version of the graphene. The detailed discussions of this ground-state phase of Na_3Bi can be referred to Ref. 67-70.

At 0.8 GPa, a pressure induced phase transition occurs from the ground state *hP*24 phase to a cubic *cF*16-Na_3Bi (space group of $Fm\bar{3}m$), as shown in Fig. 3(a and e). This agrees with the experimental measured phase transition pressure range, 0.7-1.0 GPa[92, 113, 114]. For the *cF*16-Na_3Bi at 1.0 GPa the optimized crystal structure is visualized in Fig. 3(a) and the derived phonon dispersion in Fig. 3(c) exhibits no any imaginary frequencies, evidencing its dynamical stability. It is clear that this cubic Na_3Bi crystalizing in a BiF_3-type structure with a = 7.550 Å. The Bi atoms lie at 4*b* site (0.5, 0.5, 0.5) and the Na atoms occupy two inequivalent sites, 4*a* (0, 0, 0) and 8*c* (3/4, 3/4, 3/4), as compiled in Table 1. The Na1-Bi interatomic distance is 3.775 Å while the Na2-Bi distance is relatively smaller, about 3.269 Å.

With increasing the pressure above 118 GPa, the relative enthalpies between the *cF*16 and *oC*16 phases in Fig. 3(f) demonstrate a phase transformation from the *cF*16 phase to an orthorhombic *oC*16 phase. The optimized lattice parameters and atomic sites for *oC*16-Na_3Bi are listed in Table 1. For this *oC*16 phase, there are also two inequivalent Na atomic sites at 4*c* (0, 0.6997, 0.25) and 8*f* (0, 0.1114, 0.0599), respectively, and the Bi atoms at 4*c* (0, 0.3991, 0.25). It is interesting to note that the *oC*16 phase is a layered structure, in which the Na1 and Na2 atoms form five-membered rings and they are simultaneously separated by the zigzag Bi lines in each layer. The Na1-Na2 distance within the same layer is about 2.341 Å, whereas the distance between the adjacent layers is relatively smaller, about 2.317 Å, which is comparable with the Na-Na distance in the *cI*16-Na, from 2.319 Å to 2.433 Å at 120 GPa. We have also calculated its phonon dispersion curves (Fig. 3(d)), indicating its vibrational stabilities. Note that the *cF*16-

Na_3Bi is also calculated to be dynamically stable at zero pressure.

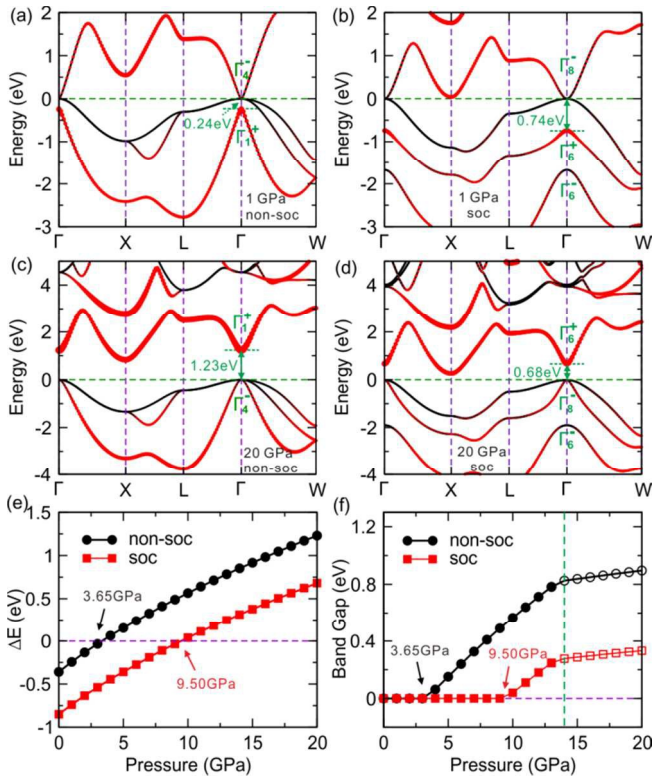

Figure 4. (Color online) The electronic band structure for *cF*16-Na_3Bi at 1 GPa (a, b) and 20 GPa (c, d) without and with SOC. The red solid circles indicate the projection to the Na-3*s* states. The band-gap and the energy difference of Na-3*s* and Bi-6*p* states as a function of pressure are represented in (e) and (f). Note that the solid circles and squares denote the direct band-gap, while the open circles and squares represent the indirect band-gap in (e).

4.1.2. Electronic structures

In different from the ground-state *hP*24 phase with unique feature of 3D TDS[52-54,57], the cubic *cF*16 phase of Na_3Bi exhibits other attractive electronic properties. As presented in Fig. 4(a and b), it is clear that the *cF*16-Na_3Bi is a topological semimetal at 1 GPa as its conduction and valence bands touch only at the Γ point and it processes the inverted band ordering simultaneously, no matter whether the spin-orbit coupling effect (SOC) is included. In the case without the SOC effect (Fig. 4(a)), the Fermi level exactly crosses the threefold degenerated Bi-$p_{(x,y,z)}$ states at Γ. However, when the SOC is considered, the threefold degenerated Bi-$p_{(x,y,z)}$ states (Γ_4) are further split into the doubly degenerated Γ_8 and Γ_6 states and the Γ_8 still exactly touches the Fermi level. From Fig. 4(a), we found the Na-3*s* states are energetically lower by about 0.24 eV than the Bi-6*p* states (Γ_4) at the Γ point without the SOC effect and this difference is further enhanced to 0.74 eV with the SOC effect (Fig. 4(b)). The inverted band feature, which is often deemed as the prerequisite of the nontrivial topological insulators, is extremely important because the Na-3*s* and Bi-6*p* states at Γ exhibit opposite parities, as shown in Fig. 4(a and b). However, noted that no any other band inversions occur for the rest high symmetric points in the BZ. Our calculations further revealed that the band inversion at Γ is obviously caused by the crystal field effect with the protection of lattice symmetry, rather than the chemical doping, pressure or strains. This is found similar to the famous case of HgTe[115], which is a promising material in the type-III quantum well for quantum spin hall effect and it also exhibits an nearly zero direct band gap at Γ point in the BZ and an analogous inverted band ordering.

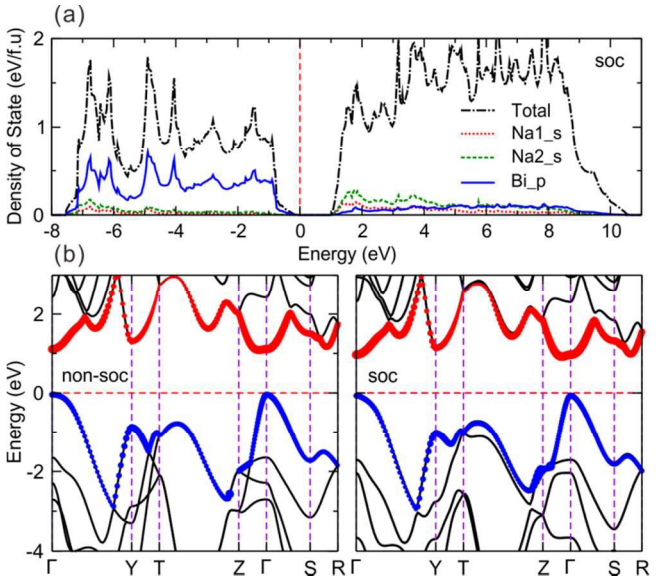

Figure 5. (Color online) The calculated electronic structures of the *oC*16-Na_3Bi at 120 GPa: (a) the total and partial density of states (PDOS) with SOC and (b) the band structures without (left) and with (right) the SOC. The red and blue solid circles indicate the projection to the Na-3*s* and Bi-6*p* states, respectively.

With further increasing the pressure under hydrostatic compression, we have observed a pressure-induced phase transition to a trivial band-gap insulator for the *cF*16-Na_3Bi, as evidenced in Fig. 4(c and d). The transition critical pressure (P_C) is further determined by analyzing the energy difference between the Na-3*s* and Bi-6*p* states at Γ without the SOC effect,

$$\Delta E(\text{non-soc}) = E(\Gamma_1) - E(\Gamma_4) \quad (1)$$

and, with the SOC inclusion

$$\Delta E(\text{soc}) = E(\Gamma_6) - E(\Gamma_8) \quad (2)$$

When ΔE is negative, an inverted band order can be observed. In contrast, if ΔE is positive, the normal band order appears. As illustrated in Fig. 4(e), our calculations revealed that the critical P_C is 3.65 GPa without the SOC effect and, if the SOC effect is included the P_C increases to 9.50 GPa. When $P < P_C$, the inverted band order between the Na-3*s* states and Bi-6*p* states remains and *cF*16-Na_3Bi is a topological semimetal. Once $P > P_C$, the normal band order occurs so that *cF*16-Na_3Bi becomes a direct band-gap insulator and the band gap increases with the rising pressure (Fig. 4(f)). At $P > 14$ GPa, the *cF*16-Na_3Bi becomes an indirect band-gap insulator because the lowest conduction band at *X* is lower in energy than that at Γ (namely, the Γ_8 state). For instance, at 20 GPa the band structure shows normal band ordering in Fig. 4(c and d) because the Na-3*s* state lies above the Bi-6*p* state by about 1.23 eV and 0.68 eV without

and with the SOC effect, respectively. Our calculation also reveals that the band gap of the *cF*16 phase of Na_3Bi monotonously increases up to 1.43 eV at 118 GPa. Due to the well-known reason, the standard DFT calculations always underestimate the band gap. In reality, it can be expected that the real band gap should be larger than those current derived data.

Above 118 GPa, this *cF*16-Na_3Bi can be transformed into an *oC*16 one, as accompanied with the appearance of a relatively wide band gap. As evidenced in Fig. 5(a), the electronic densities of states (DOSs) and the band structures at 120 GPa demonstrate that the *oC*16 phase is a normal band insulator. Without the SOC effect, the band gap is about 1.1 eV. We also found that the SOC inclusion only slightly reduces the band gap to 0.97 eV. The Na-3*s* and Bi-6*p* states dominates the conduction and valence bands, respectively, which are in contrast with other three low-pressure Na_3Bi phases (*hP*8[67], *hP*24[70] and *cF*16). Our calculations also demonstrated that the conventional band insulating state of this *oC*16 phase can remain up to at least 160 GPa.

4.2. NaBi

4.2.1. Structural stability and phonon dispersion

The crystal structure of NaBi was firstly interpreted by Zintl *et al*[93] through the powder X-ray pattern to crystallize in a tetragonal structure, *tP*2 (space group *P*4/*mmm*), with two atoms per unit cell (Fig. 6(a)). Our evolutionary searches reveal exactly the same ground-state structure, with the *c*/*a* ratio of 1.43. The calculations also demonstrated that NaBi undergoes a structural phase transformation from the ground-state *tP*2 phase to the cubic *cP*2 one (Fig. 6(b)) with the increasing pressure. Interestingly, the high-pressure *cP*2 phase is indeed closely correlated with the *tP*2 one. Their optimized lattice parameters and atomic sites are presented in Table 1, as compared with available experimental data. As the pressure rising, both the lattice constants of *tP*2-NaBi, show negative dependencies of pressure (Fig. 6(c)). At pressures above 36 GPa, the cubic *cP*2 phase become energetically more stable than the tetragonal *tP*2 structure, thus leading to $a = c$ (Fig. 6(c and d)). From the calculated phonon dispersion curves (Fig. 6(e and f)), it is clear that the *tP*2 and *cP*2 structures are both dynamically stable at ambient pressure and 40 GPa, respectively.

4.2.2. Electronic structure

Most recently, we have found that the ground-state *tP*2 phase of NaBi is an intrinsic 3D topological metal with the combined properties of the electron-phonon coupling superconductivity (with the estimated T_C = 1.82-2.59 K[81] in nice agreement with recent experimental measurements[83]) and the obviously anisotropic but extremely low thermal conductivity. The detailed results and discussions can be referred to Ref. 81.

At high pressure, the stable *cP*2 phase is a normal metal, as illustrated by its electronic densities of states and band structures in Fig. 6(g). It can be seen that the total DOS at the Fermi level is about 0.53 states eV^{-1} $f.u.^{-1}$, mainly from the Bi-6*p* states. The isolated lowest band around -15 eV ~ -10 eV is originated by Bi-6*s* orbitals. Most of the Na-3*s* states are unoccupied, lying at the high energetic antibonding regions, while partial Bi-6*p* states stay in the occupied bonding regions below the Fermi level. Comparing the band structures with and without the effect of SOC, the SOC does not obviously alter the band occupations, just splitting the threefold degenerated Bi-$p_{(x,y,z)}$ states at Γ point and separating an overlapped band.

As what we have performed for the *tP*2-NaBi, we have also utilized the linear response theory and fine k and q meshes[116] to calculate the Eliashberg function ($\alpha^2F(\omega)$) and the strength of the electron-phonon (*e*-ph) coupling ($\lambda(\omega)$) for the high-pressure *cP*2 phase. At 40 GPa, the Eliashberg function integrates to a low *e*-ph coupling strength λ = 0.25 and the relatively low logarithmic average $\langle\omega_{ln}\rangle$ = 130.1 cm^{-1}. This λ is only one third of the *tP*2 phase[81], whereas the $\langle\omega_{ln}\rangle$ in the *cP*2 phase is three times larger than that of the *tP*2 phase (40.9 cm^{-1}). Using the Allen-Dynes formula[117] and the typical μ of 0.14-0.10 we have further estimated the T_C in the *cP*2 phase at 40 GPa to be 0.006 K, obviously indicating its non-superconducting feature. Even up to 100 GPa, the λ and $\langle\omega_{ln}\rangle$ are further derived to be 0.23 and 180.7 cm^{-1}, respectively, also implying no superconductivity.

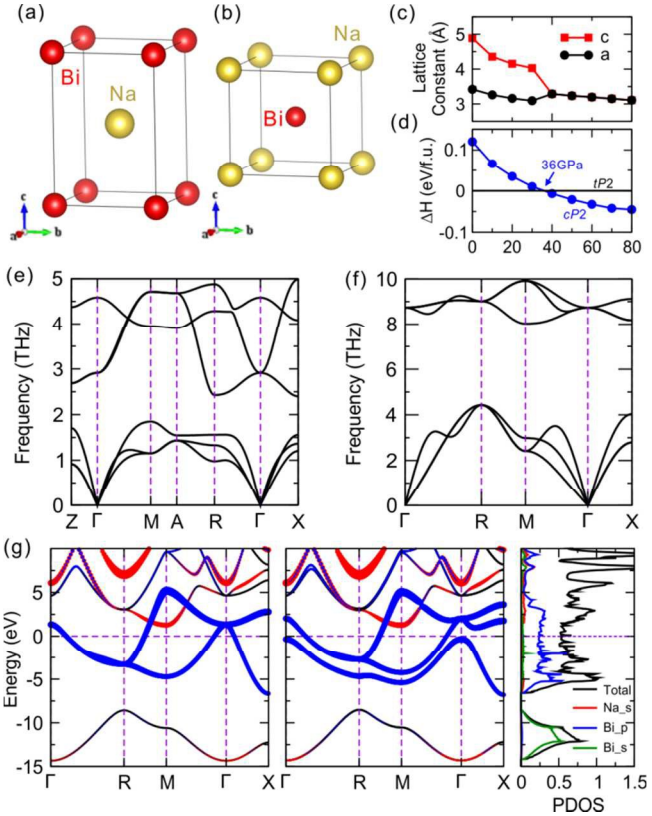

Figure 6. (Color online) The crystal structure of (a) *tP*2-NaBi at ambient pressure and (b) *cP*2-NaBi at 40 GPa. The lattice constant of NaBi and the relative enthalpy as a function of pressure are presented in (c) and (d), respectively. The phonon dispersion curves for both structures are shown in (e) and (f). The calculated band structures without (left) and with (middle) SOC for *cP*2-NaBi at 40 GPa are illustrated in (g), as well as the DOS with SOC (right). The red and blue solid circles denote the projection to the Na-3*s* and Bi-6*p* states, respectively.

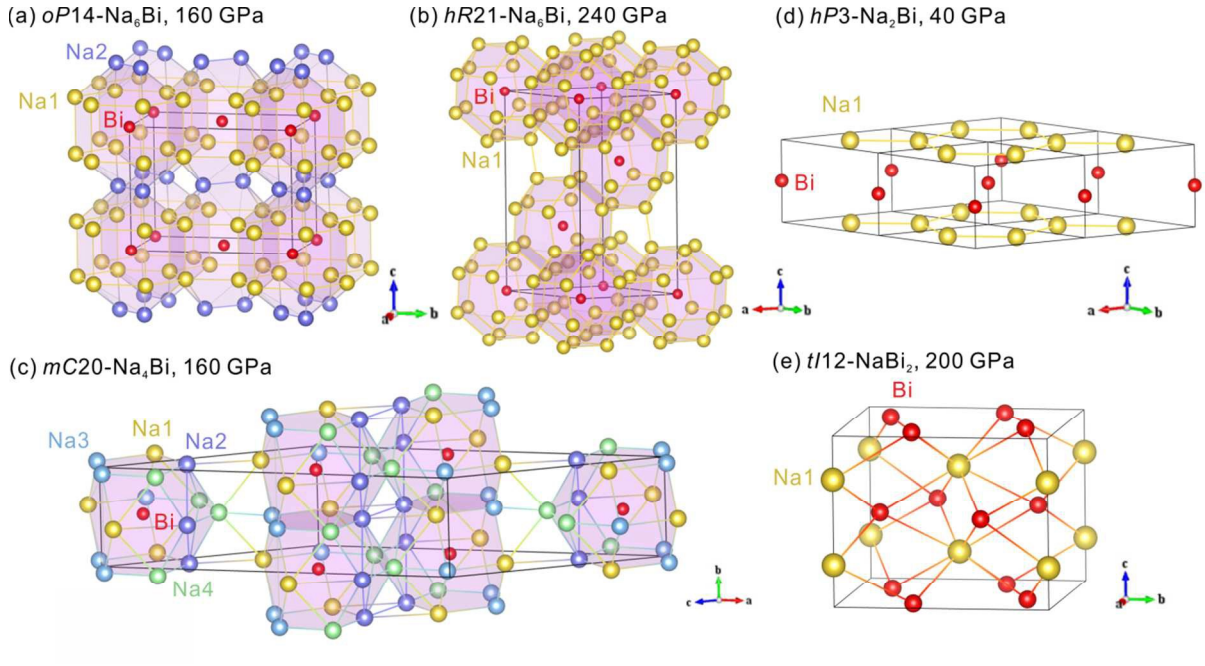

Figure 7. (Color online) The predicted high pressure phases of the binary Na-Bi system. (a) *oP*14-Na_6Bi at 160 GPa, (b) *hR*21-Na_6Bi at 240 GPa, (c) *mC*20-Na_4Bi at 160 GPa, (d) *hP*3-Na_2Bi at 40 GPa in a 2×2×1 supercell and (e) *tI*12-$NaBi_2$ at 200 GPa. The red circles represent the Bi atoms while the Na atoms are shown in different colors according to their Wyckoff sites. Here, yellow, purple, blue and green circles represents Na1, Na2, Na3, and Na4 atoms, respectively.

5. Predicted compounds

At high pressures, our computed convex hull revealed several never-reported compounds, including Na_6Bi, Na_4Bi, Na_2Bi, and $NaBi_2$ (Fig. 1), which greatly enrich the phase diversity of the Na-Bi binary system. The following subsections would discuss the crystal structures and calculated electronic properties in detail.

5.1 Phase stability and crystal structure

5.1.1. Na_6Bi

For the composition of Na_6Bi, we predicted it would appear at 142.5 GPa between the tie-line of *mC*20-Na_6Bi and *cI*16-Na and it remains as a stable composition even up to 320 GPa. In the pressure range from 142.5 to 201 GPa, our evolutionary searches reveal an orthorhombic *oP*14-Na_6Bi phase with lowest-enthalpy in a *Pbam* symmetry. As illustrated in Fig. 7(a) at 160 GPa, if projected along the *a*-axis, the *oP*14-Na_6Bi is a sandwich-like structure with every three Na layers separating by one Bi atomic layer. The Na atoms hold two inequivalent atomic sites, Na1 at 8*i* (0.0150, 0.3371, 0.2252) and Na2 at 4*h* (0.1590, 0.1002, 0.5). From the projection from the *c*-axis, the Na1 atoms form irregular graphene-like layer, while every two Na2 atoms create a dimer. The distances between Na1 atoms within the same layer are ranging from 2.19 Å to 2.32 Å and the Na1-Na2 distances between the adjacent layers are about 2.03 Å to 2.19 Å at 160 GPa. However, within a Na2-dimer, the Na2-Na2 bonding is about 1.85 Å, which is much smaller than other Na-Na bondings and this bonding distance is even obviously less than that of the ground state Na phase at 160 GPa (*tI*19, around 2.15 Å) indicating a stronger bonding strength between these Na2 atoms in *oP*14-Na_6Bi. Each Bi atom is surrounded by 16 Na atoms with the interatomic distances ranging from 2.50 Å to 2.68 Å building a Bi-centered polyhedral with 22 sides, as shown in Fig. 7(a). The phonon dispersions show that this *oP*14-Na_6Bi is dynamically stable in its stable pressure range, as shown in Fig. 8(a).

At pressures above 201 GPa, we found a structural phase transition from this orthorhombic *oP*14 phase to a hexagonal *hR*21 structure, with the $R\bar{3}m$ symmetry and 21 atoms in one unit cell, as shown in Fig. 7(b). The differences of enthalpy between the *oP*14 and *hR*21 phases as a function of pressure are presented in Fig. 8(c) and the phase transition pressure can be clearly seen at 201 GPa. At the pressure range from 201 to 270 GPa, the *hR*21-Na_6Bi is predicted to be stable in the Na-Bi system referring to the calculated formation energy of *tI*19-Na and bcc-Bi, while above 270 GPa the *hP*4-Na is considered as the reference phase of Na as it is experimentally synthesized under ultra-high pressure condition[43]. The dynamical stability of this *hR*21 phase is further checked through the phonon calculation. As there is no imaginary frequency within the BZ, the *hR*21 phase can be deemed as dynamically stable in its stable pressure range (Fig. 8(b)). From Table 1, only one type Na and Bi sites can be found in *hR*21-Na_6Bi: 18*h* (0.5168, 0.4832, 0.0993) and 3*a* (0, 0, 0), respectively. Similar with the *oP*14-Na_6Bi, this *hR*21 phase is also a layered structure but there are only two Na layers between the Bi atomic layers as comparing with three Na atomic layers in the *oP*14 phase. In the *hR*21 structure, the Na atomic distances within one layer is around 2.10 Å which are generally larger than the interlayer Na-Na distances, ranging from 1.85 Å to 1.94 Å . On the other

hand, one Bi atom is surrounded by 18 Na atoms, forming an icosahedron with the top and bottom layered triangle Na_3 rings and two parallel hexagonal Na_6 rings. Therefore, this *hR*21 structure can be viewed as an assembly of $Na_{18}Bi$ units (Fig. 7(b)), where the Bi atoms form a *hR*1 lattice and they are enclosed within icosahedrons of Na. Interestingly, the similar structural feature has also been found in a predicted stable high pressure phase of Li_6B[64].

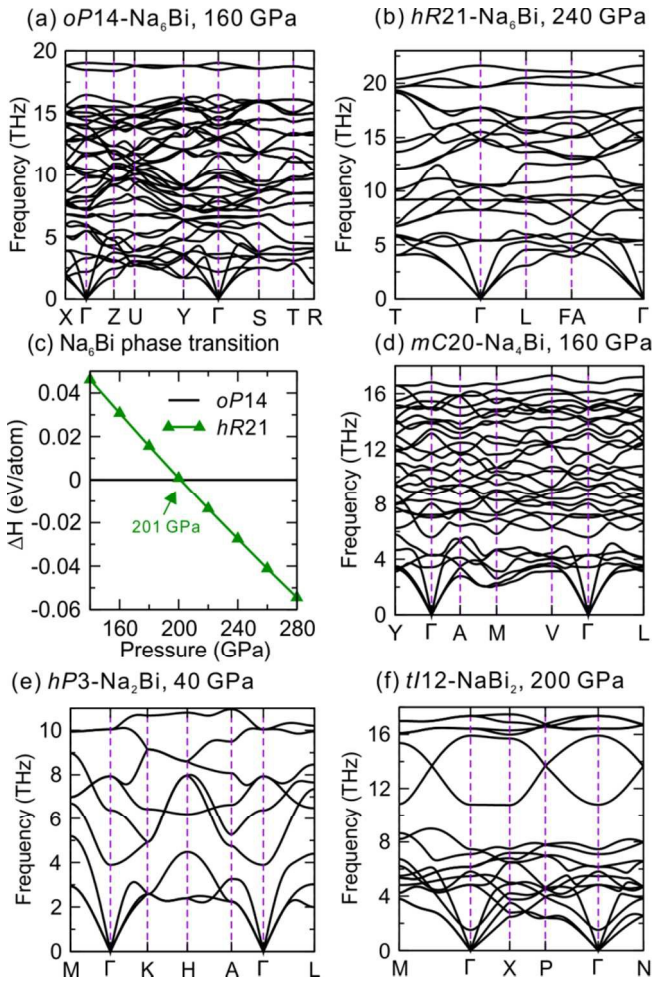

Figure 8. (Color online) The phonon dispersion curves of (a) *oP*14-Na_6Bi at 160 GPa, (b) *hR*21-Na_6Bi at 240 GPa, (d) *mC*20-Na_4Bi at 160 GPa, (e) *hP*3-Na_2Bi at 40 GPa and (f) *tI*12-$NaBi_2$ at 200 GPa. Meanwhile, the relative phase stability of two Na_6Bi structures as the function of pressure is shown in (c).

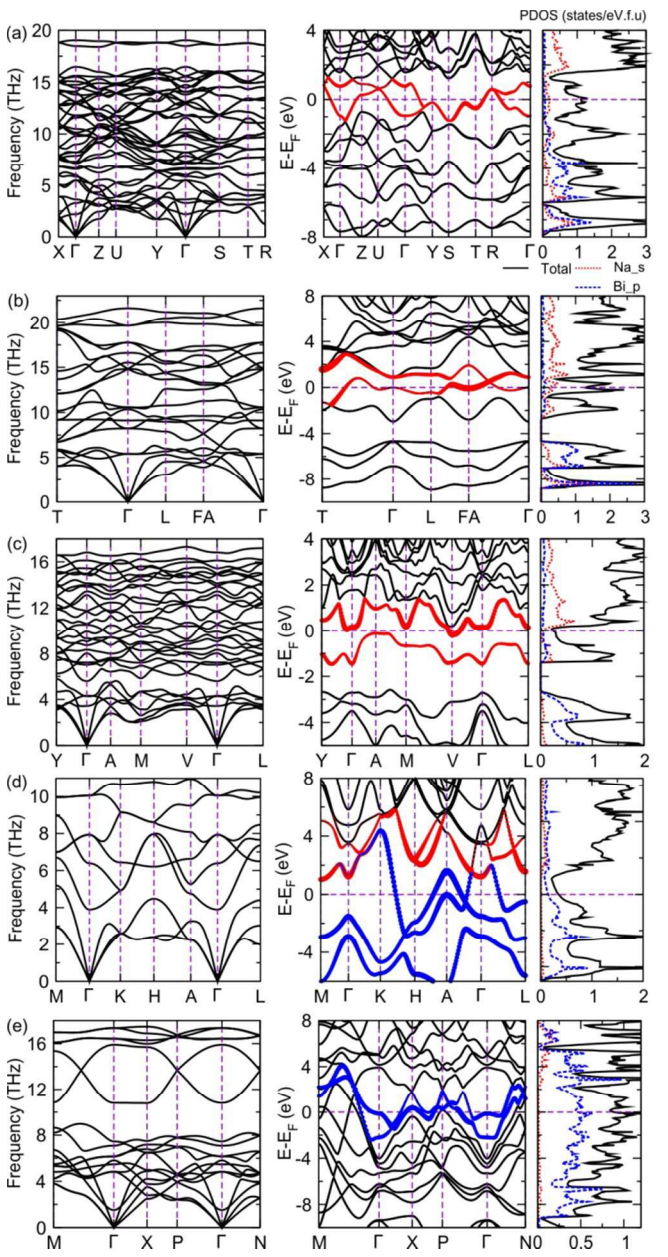

Figure 9. (Color online) The band structures without (left) and with (middle) the SOC and the total and partial density of states (right) with SOC. for (a) *oP*14-Na_6Bi at 160 GPa, (b) *hR*21-Na_6Bi at 240 GPa, (c) *mC*20-Na_4Bi at 160 GPa, (d) *hP*3-Na_2Bi at 40 GPa and (e) *tI*12-$NaBi_2$ at 200 GPa. The red and blue solid circles represent the projection to the Na-3*s* and Bi-6*p* states, respectively.

5.1.2 Na_4Bi

Na_4Bi was found stable in the pressure range of 105 GPa to 221 GPa and adopt a monoclinic *mC*20 structure (space group *C*2/*m*), as presented in Fig. 7(c) and Table 1. In the pressure range that we considered, the calculations found no any other structural phase transition for this 4:1 composition. For the *mC*20-Na_4Bi, the Na atoms occupy four inequivalent 4*i* Wyckoff sites and Bi atoms stay at one 4*i* site. There are two stacked atomic layer with the adjacent layers rotated by 29.7°with respect to each other. These two layers share very similar atomic combination feature as they both consist of two

connected five-membered Na_5 rings and one ten-membered Na_{10} ring with two centered Bi atoms. Thus, a 22-side Bi centered polyhedral is formed with top and bottom layered closed Na_5 rings and middle open Na_5 ring. This structure is demonstrated to be dynamically stable in its stable pressure ranges by the phonon calculation, as presented in Fig. 8(d).

5.1.3. Na_2Bi

The compound Na_2Bi crystallizes in a simple AlB_2-type structure (*hP*3) with the graphite-like Na sheets sandwiching closed-packed layers of Bi atoms (Table 1 and Fig. 7(d)). This compound was predicted to be stable above 38 GPa in the Na-Bi system (Fig. 1) and will remains its stability even up to 320 GPa. According this *hP*3 structure, the Na and Bi atoms stay at 2*d* (0.3333, 0.6667, 0.5) and 1*a* (0, 0, 0), respectively. At 40 GPa, the Na-Na distance within the graphite-like layer is about 2.46 Å which is slightly smaller than the shortest Na-Na bonding distance (2.677 Å) in bcc-Na at the same pressure.

5.1.4. $NaBi_2$

$NaBi_2$, the composition with the highest Bi content, was predicted to be stable above 171 GPa and it remains stable even up to 320 GPa (Fig. 1). Our evolutionary structural search evidences a tetragonal *tI*12 structure with the space group *I*4*mcm* for $NaBi_2$ in its stable pressure range from 171 GPa to 320 GPa. Figure 7(e) shows its crystal structure and its structural parameters at 200 GPa are presented in Table 1. Among all those revealed Na-Bi compounds, $NaBi_2$ is the only composition whose Bi content is over Na. From Table 1, one can see that the Na and Bi occupy two inequivalent Wyckoff sites, 4*a* (0, 0, 0.25) and 8*h* (0.1588, 0.6588, 0), respectively. If being projected along the *c*-axis, it can be clearly visualized that the Bi atoms form "4 + 8" membered rings. As seen in its unit cell, each Na atom has eight Bi coordinators with the Na-Bi distance of 2.46 Å and each Bi atom form two kinds of bonding (2.74 Å and 2.94 Å) with its four nearest neighbouring Bi atoms.

Table 2. The density of state (DOS) at Fermi Level ($N(E_F)$, [states eV^{-1} $f.u^{-1}$]) for the metallic phases of Na-Bi system at given pressure. In general, the $N(E_F)$ represent the strength of the metallicity.

Phase	Pearson symbol	Pressure	$N(E_F)$	$N(E_F)$ (soc)
Na_6Bi	*oP*14	160	1.092	1.115
	*hR*21	240	1.302	1.294
Na_4Bi	*mC*20	160	0.389	0.236
Na_2Bi	*hP*3	40	0.458	0.349
NaBi	*tP*2	0	0.846	0.527
	*cP*2	40	0.508	0.532
$NaBi_2$	*tI*12	200	0.908	0.885

5.2 Electronic structures

We have calculated the electronic band structures and densities of states (DOSs) for all those compounds of Na_6Bi, Na_4Bi, Na_2Bi and $NaBi_2$ at selected pressures, as illustrated in Fig. 9. The common features from their band structures and the DOSs can be observed. At the pressures considered here, all those compounds are typical metallic, no matter whether the SOC effect is included. The DOS at the Fermi level ($N(E_F)$) are dominated by Na-3*s* states for Na_6Bi, Na_4Bi and Na_2Bi, whereas the $N(E_F)$ for $NaBi_2$ is mainly from both Na-3*s* and Bi-6*p* states. We have further calculated the corresponding $N(E_F)$ as compiled in Table 2. Among them, the SOC effect exhibits the highest impact on the *tP*2-NaBi by reducing the $N(E_F)$ about 0.319 states eV^{-1} $f.u.^{-1}$ with respect to the case without the inclusion of SOC. As for *cP*2-NaBi, although they belong to the same composition and have similar crystal structure, the change of the $N(E_F)$ is so slight (only 0.024 states eV^{-1} $f.u.^{-1}$) that we can neglect the SOC effect. In particular, for Na_4Bi and Na_2Bi, the SOC effect also lower the $N(E_F)$ by 0.153 and 0.109 states eV^{-1} $f.u.^{-1}$, respectively. For other compounds of Na_6Bi and $NaBi_2$, the SOC shows almost no influence in their $N(E_F)$.

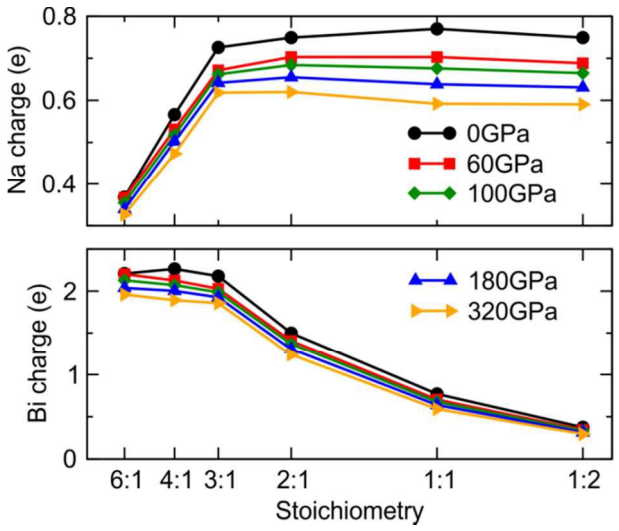

Figure 10. (Color online) The calculated Bader charge of Na and Bi in the Na-Bi systems at different pressures. The predicted most stable structures at 180 GPa for different Na-Bi compositions are used for the Bader charge calculation.

6. The nature of bonding

It is well-known that among all elements, Na has a very low electronegativity (0.9 eV), whereas Bi has a relatively large electronegativity (1.9 eV). When Na mixes with Bi to form compounds, it is reasonable to expect that Na often loses its valence electrons with a positive oxidation state (the maximum value of 1+ due to its outermost $3s^1$ configuration) and Bi will easily attract the valence electrons from Na to form the negative oxidation state (the most negative oxidation state of 3- according to the outermost configuration of $6s^26p^3$). Therefore, from the viewpoint of electronegativity, the Na_3Bi would be the compound easily formed in the Na-Bi system within the ionic configuration. As expected, Na_3Bi is one of the stable compounds at ambient condition. Our Bader charge analysis reveals that Na loses the valence charge of 0.72 to form cationic $Na^{0.72+}$, whereas Bi attracts the valence charges of 2.16 to create anionic $Bi^{2.16-}$ in the Na_3Bi compound. In particular, the cation and anion should be Na^+ and Bi^- at ambient condition, respectively. This discrepancy is mainly due to the method of the Bader's technique, which calculates the charges surrounding every atom through the partitioning spaces by

identifying the zero-flux surfaces. For example, even for the typical ionic compound of NaCl, the Bader's charge analysis also reveals a non-integer transferred charge value of 0.83 from Na to Cl[64] for which this value would have been an integer of 1. In addition, for Na_3Bi, the transferred charges from Na to Bi decrease with the increasing pressure through our Bader's analysis in Fig. 10. At 100 GPa, Na loses its valence charge about 0.66, which is smaller by almost 8% comparing with the value of 0 GPa. This fact implies the existence of partial charge transfer, giving rise to the non-integer valence charge states for both Na and Bi.

Furthermore, we have systemically derived the valence charges for all compounds in the Na-Bi system as a function of pressure in Fig. 10 through the Bader's calculations. Note that we have compiled the ch arge states of the compounds with the corresponding structures which are stable at 180 GPa according to the convex hull as shown in Fig. 1(a), namely, *oP*14-Na_6Bi, *mC*20-Na_4Bi, *oC*16-Na_3Bi, *hP*3-Na_2Bi, *cP*2-NaBi and *tI*12-$NaBi_2$. Although those selected structures may not be stable at other pressures, we have checked that their structure-dependent charge states only slightly vary at the same composition. For the sake of easier comparison, the purpose of keeping same structure type for all pressure ranges investigated here would be preferable. Firstly, it has been found an obvious transition point of the charge state for both Na and Bi at the 3:1 composition. Before the composition 3:1, the transferred charges from Na increase sharply with the increasing Bi content, while after this composition the transferred charges remain relatively constant upon the different compositions. In contrast, the charge state for each Bi atom exhibits an opposite trend: with increasing the Bi content, the received charge of Bi continuously decreases. This can be easily understood due to the increased Bi content which consumes the constant transferred charges from Na. Secondly, our Bader charge analysis suggested a common phenomenon for these compounds of the non-integer partial charge transfer from Na to Bi. From Fig. 10, the transferred charges from each Na atom are smaller than 1 for all compounds. In particular, for both *oP*14-Na_6Bi and *mC*20-Na_4Bi the transferred charges for each Na atom are very small, just about 0.37 and 0.57 at 0 GPa, respectively, and the transferred values are even smaller with the increasing pressure.

In particular, for both Na_6Bi and Na_4Bi the situations of the charge transfers are highly complicated. As illustrated in Fig. 7(a) for *oP*14-Na_6Bi, there are eight Na1 and four Na2 atoms in its unit cell. The Bader's calculations demonstrated that the transferred charge values from each Na1 and Na2 are 0.25 and 0.53, respectively. Interestingly, in the cage formed by Na1 and Na2 atoms we have observed a large charge localization in its interstitial space (Fig. 12(a)), as evidenced in the calculated electronic localized function (ELF). The ELF represents the extent of electronic localization in a range from 0 to 1. If the ELF ≈ 0, it shows that the electrons are highly delocalized, whereas with ELF ≈ 1, it indicates the highly localized electrons, often denoting as lone-pair electrons or covalent

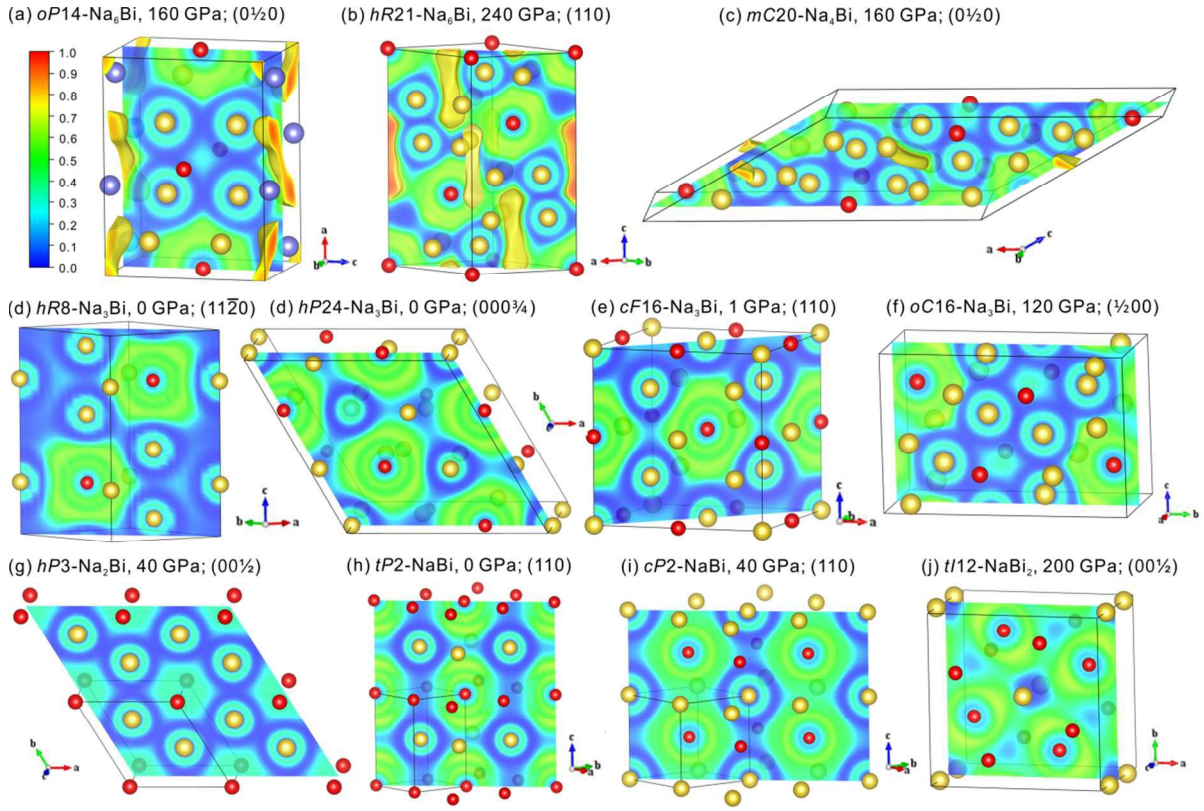

Figure 11. (Color online) The electronic localization function (ELF) for Na-Bi compounds. The yellow isosurface represents an ELF value of 0.7. The yellow and red spheres represent Na and Bi atoms, respectively. (a) The $(0\frac{1}{2}0)$ plane for *oP*14-Na_6Bi at 160 GPa, (b) (110) plane for *hR*21-Na_6Bi at 240 GPa, (c) $(0\frac{1}{2}0)$ plane for *mC*20-Na_4Bi at 160 GPa, (d) $(11\bar{2}0)$ plane for *hP*8-Na_3Bi at 0 GPa, (e) $(000\frac{3}{4})$ plane for *hP*24-Na_3Bi at 0 GPa, (e) (110) plane for *cF*16-Na_3Bi at 1 GPa, (f) $(\frac{1}{2}00)$ plane for *oC*16-

Na_3Bi at 120 GPa, (g) $(00\frac{1}{2})$ plane for *hP*3-Na_2Bi at 40 GPa, (h) (110) plane for *tP*2-NaBi at 0 GPa, (i) (110) plane for *cP*2-NaBi at 40 GPa and (j) $(00\frac{1}{2})$ plane for tI12-NaBi2 at 200 GPa. Note that a 2×2×1 supercell is used for *hP*3-Na_2Bi in (g) and the 2×2×2 supercells of *tP*2-NaBi and *cP*2-NaBi are shown in (i) and (j), respectively

bonding. In this case of *oP*14-Na_6Bi at 160 GPa, as illustrated in Fig. 11(a) and Fig. 12(a), it can be seen the emergence of electronic localizations at those interstitial spaces of Na1 and Na2 atoms with the highest ELF of 0.8. However, this fact cannot be denoted as the formation of covalent bonding or lone-pair electrons, as their shapes and positions, i.e. spherical and atomic surrounding, are not suitable with the present cases. In fact, this localized charge may be directly correlated with the high pressure and the close-packed Na cages. This phenomenon is not unique in alkali metals. For Li and Na[41, 43], it was proved that the obvious interstitial valence electron localizations exist in the lattice, even driving the structural transitions to semiconductors or insulators under high pressures. Because of the existence of the interstitial charge localizations, the charge transfer in the Na_6Bi case not only include the part from Na to Bi, but also contain the aspect from Na to the interstitial space. Our calculations still found that, with the increasing pressure, the interstitial charge localization in the cage formed by both Na1 and Na2 atoms become more obvious. This similar situation has also been observed in the case of *hR*21-Na_6Bi at 240 GPa and *mC*20-Na_4Bi at 160 GPa, as illustrated in Fig. 11(b and c) and Fig. 12(b).

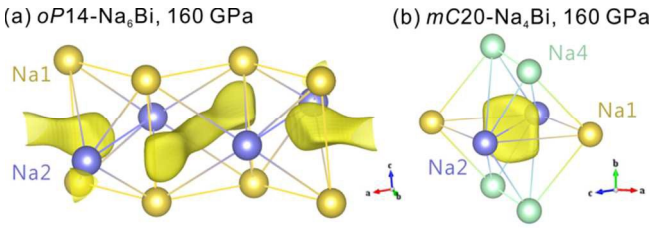

Figure 12. The partial electronic localization function (ELF) for (a) *oP*14-Na_6Bi and (b) *mC*20-Na_4Bi at 160 GPa. The yellow isosurface represents an ELF value of 0.7. In similarity with Fig. 7, the Na atoms are shown in different color according to their Wyckoff sites.

For all other compounds at their corresponding stable structures, we have not observed any interstitial charge localizations as illustrated in Fig. 11(d to j). This origin can be attributed to two facts. On the one hand, all these compounds are layered with the stacking sequence of every Na layer separated by one Bi layer. This feature results in no possibility to form the close-packed Na cages. In contrast, the Na cages can be clearly seen for both Na_6Bi and Na_4Bi (Fig. 7). On the other hand, the Na content decreases in these compounds, thereby no sufficient valence charges can be transferred from Na as compared with Na_6Bi and Na_4Bi. From Fig. 11(d to j), the ELF values surrounding Bi atom are about 0.5, while the electrons near Na atoms are relatively delocalized with the ELF value close to 0.2. This fact indicates the probable formation of the electron-gas-like states between Na and Bi.

7. Conclusion

Using the first-principles calculations coupled with the evolutionary structure search, we have systematically investigated the phase stabilities, the crystal structures and the corresponding electronic properties as well as bonding natures of the binary Na-Bi system at ambient and high pressures.

Firstly, our calculations have reproduced well the experimentally known stable compounds of NaBi and Na_3Bi for the Na-Bi system at ambient condition and yielded the corrected pressure-induced phase transformations for pure solids of Na and Bi, which are in nice agreement with the previous theoretical and experimental investigations.

Secondly, for the known stable compounds NaBi and Na_3Bi our calculations have revealed their phase transitions with increasing pressure. The NaBi has been found to undergo the structural phase transition from the ambient tetragonal phase to a cubic one above 36 GPa, while the Na_3Bi first transforms to a cubic phase above 0.8 GPa in agreement with the experimental measurements and finally goes to an orthorhombic phase above 118 GPa. In particular, the cubic Na_3Bi phase exhibits unique electronic properties with the inverted band ordering and threefold *p*-electron degeneracy at Γ. This feature is very similar to HgTe, which is a promising candidate of quantum Hall effect systems.

Thirdly, upon the increase pressure our calculations have still predicted four never-reported stable compounds of Na_6Bi, Na_4Bi, Na_2Bi and $NaBi_2$ which have been found to be stable above 142.5 GPa, 105 GPa, 38 GPa and 171 GPa, respectively, and may be experimentally synthesizable over a wide range of pressures. Interestingly, these four compounds exhibit two common features: *i*) they are all layered structure and *ii*) all these compounds can be understood via the ionic framework with metallic nature.

At last, we have systematically analysed the bonding features and the electron localized functionals for these compounds in detail. Through the Bader charge analysis, a common charge transfer from Na to Bi has been revealed. However, for *oP*14-Na_6Bi at 160 GPa, *hR*21-Na_6Bi at 240 GPa and *mC*20-Na_4Bi at 160 GPa, there exist large interstitial charge localizations in the Na atomic cages, which may associated with the high pressure and the close-packed Na environment. In addition, it is interesting to mention that a study of the most relevant meta-stable modifications and their structural and electronic properties is being undertaken across a wide range of pressure.

Acknowledgment

This work was supported by the "Hundred Talents Project" of the Chinese Academy of Sciences and from the Major Research Plan (Grand Number: 91226204), the Key Research Program of Chinese Academy of Sciences (Grant No. KGZD-EW-T06), the NSFC of China (Grand Numbers: 51474202 and 51174188) and Beijing Supercomputing Center of CAS (including its

Shenyang branch) as well as Vienna Supercomputing Center (VSC cluster).

Notes and references

[a] Shenyang National Laboratory for Materials Science, Institute of Metal Research, Chinese Academy of Sciences, Shenyang, 110016, China.

1 J. Greeley, T. F. Jaramillo, J. Bonde, I. B. Chorkendorff and J. K. Norskov, *Nat. Mater.*, 2006, **5**, 909-913.
2 S. Curtarolo, G. L. W. Hart, M. B. Nardelli, N. Mingo, S. Sanvito and O. Levy, *Nat. Mater.*, 2013, **12**, 191-201.
3 A. Jain, G. Hautier, C. J. Moore, S. Ping Ong, C. C. Fischer, T. Mueller, K. A. Persson and G. Ceder, *Comput. Mat. Sci.*, 2011, **50**, 2295-2310.
4 W. Setyawan and S. Curtarolo, *Comput. Mat. Sci.*, 2010, **49**, 299-312.
5 M. Asta, *JOM*, 2014, **66**, 364-365.
6 S. M. Woodley and R. Catlow, *Nat. Mater.*, 2008, **7**, 937-946.
7 J. K. Norskov, T. Bligaard, J. Rossmeisl and C. H. Christensen, *Nat. Chem.*, 2009, **1**, 37-46.
8 K. Lejaeghere, S. Cottenier and V. Van Speybroeck, *Phys. Rev. Lett.*, 2013, **111**, 075501.
9 J. C. Schön and M. Jansen, *Z. Kristallogr.*, 2001, **216**, 307-325.
10 A. R. Oganov and C. W. Glass, *J. Chem. Phys.*, 2006, **124**, 244704.
11 A. R. Oganov, A. O. Lyakhov and M. Valle, *Acc. Chem. Res.*, 2011, **44**, 227–237.
12 S. Curtarolo, W. Setyawan, G. L. W. Hart, M. Jahnatek, R. V. Chepulskii, R. H. Taylor, S. Wang, J. Xue, K. Yang, O. Levy, M. J. Mehl, H. T. Stokes, D. O. Demchenko and D. Morgan, *Comput. Mat. Sci.*, 2012, **58**, 218-226.
13 C. J. Pickard and R. J. Needs, *J. Phys. Condens. Matter.*, 2011, **23**, 053201.
14 A. N. Kolmogorov, **http://maise-guide.org**.
15 Y. Wang, J. Lv, L. Zhu and Y. Ma, *Comput. Phys. Commun.,*, 2012, **183**, 2063-2070.
16 J. C. Schön and M. Jansen, *Angew. Chem. Int Ed. Engl.*, 1996, **35**, 1286-1304.
17 M. R. Farrow, Y. Chow and S. M. Woodley, *Phys. Chem. Chem. Phys.*, 2014, **16**, 21119-21134.
18 J. Maddox, *Nature*, 1988, **335**, 201.
19 J. Pannetier, J. Bassas-Alsina, Rodriguez-Carvajal and C. J., V. , *Nature*, 1990, **346**, 343-345.
20 D. Deaven and K. Ho, *Phys. Rev. Lett.*, 1995, **75**, 288-291.
21 S. Curtarolo, D. Morgan, K. Persson, J. Rodgers and G. Ceder, *Phys. Rev. Lett.*, 2003, **91**.
22 R. Drautz, A. Díaz-Ortiz, M. Fähnle and H. Dosch, *Phys. Rev. Lett.*, 2004, **93**, 067202.
23 J. C. Schön, *Z. Anorg. Allg. Chem.* , 2004, **630**, 2354-2366.
24 J. C. Schön and M. Jansen, *Int. J. Mater. Res.*, 2009, **100**, 135-152.
25 S. M. Woodley and C. R. A. Catlow, *Comput. Mat. Sci.*, 2009, **45**, 84-95.
26 M. Jansen, K. Doll and J. C. Schon, *Acta Crystallogr A*, 2010, **66**, 518-534.
27 I. V. Pentin, V. Saltykov, J. Nuss, J. C. Schön and M. Jansen, *Chem-A Euro J.*, 2012, **18**, 3559-3565.
28 J. Reedijk and K. Poeppelmeier, eds., *Comprehensive Inorganic Chemistry II*, Elsevier Science BV, Amsterdam, 2013.
29 V. Sharma, C. Wang, R. G. Lorenzini, R. Ma, Q. Zhu, D. W. Sinkovits, G. Pilania, A. R. Oganov, S. Kumar, G. A. Sotzing, S. A. Boggs and R. Ramprasad, *Nat. Commun.*, 2014, **5**, 4845.
30 Y. Wang and Y. Ma, *J. Chem. Phys.*, 2014, **140**, 040901.
31 Q. Zhu, A. R. Oganov and X. F. Zhou, *Top Curr. Chem.*, 2014, **345**, 223-256.
32 N. L. Allan, G. D. Barrera, M. Y. Lavrentiev, I. T. Todorov and J. A. Purton, *J. Mater. Chem.*, 2001, **11**, 63-68.
33 S. P. Ong, L. Wang, B. Kang and G. Ceder, *Chem. Mater.*, 2008, **20**, 1798-1807.
34 X. Y. Cheng, W. Zhang, X.-Q. Chen, H. Y. Niu, P. T. Liu, K. Du, G. Liu, D. Z. Li, H.-M. Cheng, H. Q. Ye and Y. Y. Li, *Appl. Phys. Lett.*, 2013, **103**, 171903.
35 X. Y. Cheng, X. Q. Chen, D. Z. Li and Y. Y. Li, *Acta Crystallogr. C Struct. Chem.*, 2014, **70**, 85-103.
36 H. Y. Niu, X. Q. Chen, W. Ren, Q. Zhu, A. R. Oganov, D. Z. Li and Y. Y. Li, *Phys. Chem. Chem. Phys.*, 2014, **16**, 15866-15873.
37 A. N. Kolmogorov, S. Shah, E. R. Margine, A. F. Bialon, T. Hammerschmidt and R. Drautz, *Phys. Rev. Lett.*, 2010, **105**, 217003.
38 A. Hermann, N. W. Ashcroft and R. Hoffmann, *Inorg. Mater.* , 2012, **51**, 9066-9075.
39 Q. Zeng, J. Peng, A. R. Oganov, Q. Zhu, C. Xie, X. Zhang, D. Dong, L. Zhang and L. Cheng, *Phys. Rev. B*, 2013, **88**, 214107.
40 A. G. Van Der Geest and A. N. Kolmogorov, *Calphad*, 2014, **46**, 184-204.
41 T. Matsuoka and K. Shimizu, *Nature*, 2009, **458**, 186-189.
42 Y. Ma, A. Oganov and Y. Xie, *Phys. Rev. B*, 2008, **78**, 014102.
43 Y. Ma, M. Eremets, A. R. Oganov, Y. Xie, I. Trojan, S. Medvedev, A. O. Lyakhov, M. Valle and V. Prakapenka, *Nature*, 2009, **458**, 182-185.
44 A. R. Oganov, J. Chen, C. Gatti, Y. Ma, C. W. Glass, Z. Liu, T. Yu, O. O. Kurakevych and V. L. Solozhenko, *Nature*, 2009, **457**, 863-867.
45 A. R. Oganov, Y. Ma, Y. Xu, I. Errea, A. Bergara and A. O. Lyakhov, *Proc. Natl. Acad. Sci. U. S. A.*, 2010, **107**, 7646-7651.
46 A. R. Oganov and S. Ono, *Nature*, 2004, **430**, 445-448.
47 Q. Zhu, A. R. Oganov and A. O. Lyakhov, *Phys. Chem. Chem. Phys.*, 2013, **15**, 7696-7700.
48 B. Militzer and H. F. Wilson, *Phys. Rev. Lett.*, 2010, **105**.
49 M. Ji, K. Umemoto, C.-Z. Wang, K.-M. Ho and R. M. Wentzcovitch, *Phys. Rev. B*, 2011, **84**, 220105.
50 Y. Wang, H. Liu, J. Lv, L. Zhu, H. Wang and Y. Ma, *Nat. Commun.*, 2011, **2**, 563.
51 A. Hermann, N. W. Ashcroft and R. Hoffmann, *Proc. Natl. Acad. Sci. U. S. A.*, 2012, **109**, 745.
52 C. J. Pickard, M. Martinez-Canales and R. J. Needs, *Phys. Rev. Lett.*, 2013, **110**, 245701.
53 G. Gao, A. Oganov, A. Bergara, M. Martinez-Canales, T. Cui, T. Iitaka, Y. Ma and G. Zou, *Phys. Rev. Lett.*, 2008, **101**, 107002.
54 G. Gao, A. R. Oganov, P. Li, Z. Li, H. Wang, T. Cui, Y. Ma, A. Bergara, A. O. Lyakhov, T. Iitaka and G. Zou, *Proc. Natl. Acad. Sci. U. S. A.*, 2010, **107**, 1317-1320.
55 Y. Li, G. Gao, Y. Xie, Y. Ma, T. Cui and G. Zou, *Proc. Natl. Acad. Sci. U. S. A.*, 2010, **107**, 15708-15711.
56 S. Shah and A. N. Kolmogorov, *Phys. Rev. B*, 2013, **88**, 014107.
57 H. Wang, Q. Li, Y. Li, Y. Xu, T. Cui, A. Oganov and Y. Ma, *Phys. Rev. B*, 2009, **79**, 132109.
58 Q. Li, H. Wang, Y. Tian, Y. Xia, T. Cui, J. He, Y. Ma and G. Zou, *J. Appl. Phys.*, 2010, **108**, 023507.
59 E. Zurek, R. Hoffmann, N. W. Ashcroft, A. R. Oganov and A. O. Lyakhov, *Proc. Natl. Acad. Sci. U. S. A.*, 2009, **106**, 17640-17643.
60 M. S. Miao, *Nat. Chem.*, 2013, **5**, 846-852.
61 W. Zhang, A. R. Oganov, A. F. Goncharov, Q. Zhu, S. E. Boulfelfel, A. O. Lyakhov, E. Stavrou, M. Somayazulu, V. B. Prakapenka and Z. Konopkova, *Science*, 2013, **342**, 1502-1505.
62 Q. Zhu, D. Y. Jung, A. R. Oganov, C. W. Glass, C. Gatti and A. O. Lyakhov, *Nat. Chem.*, 2013, **5**, 61-65.
63 A. Hermann, A. McSorley, N. W. Ashcroft and R. Hoffmann, *J. Am. Chem. Soc.*, 2012, **134**, 18606-18618.
64 F. Peng, M. Miao, H. Wang, Q. Li and Y. Ma, *J. Am. Chem. Soc.*, 2012, **134**, 18599-18605.
65 H. Wang, S. T. John, K. Tanaka, T. Iitaka and Y. Ma, *Proc. Natl. Acad. Sci. U. S. A.*, 2012, **109**, 6463-6466.
66 G. Gao, N. W. Ashcroft and R. Hoffmann, *J. Am. Chem. Soc.*, 2013, **135**, 11651-11656.
67 Z. Wang, Y. Sun, X.-Q. Chen, C. Franchini, G. Xu, H. Weng, X. Dai and Z. Fang, *Phys. Rev. B*, 2012, **85**, 195320.
68 S. Y. Xu, C. Liu, S. K. Kushwaha, T. R. Chang, J. W. Krizan, R. Sankar and M. Z. Hasan, *arXiv:1312.7624.*, 2013.
69 Z. K. Liu, B. Zhou, Y. Zhang, Z. J. Wang, H. M. Weng, D. Prabhakaran, S. K. Mo, Z. X. Shen, Z. Fang, X. Dai, Z. Hussain and Y. L. Chen, *Science*, 2014, **343**, 864-867.
70 X. Y. Cheng, R. H. Li, Y. Sun, X.-Q. Chen, D. Z. Li and Y. Y. Li, *Phys. Rev. B*, 2014, **89**, 245201.
71 Z. Fang, N. Nagaosa, K. S. Takahashi, A. Asamitsu, R. Mathieu, T. Ogasawara, H. Yamada, M. Kawasaki and K. Terakura, *Science*, 2003, **302**, 92-95.

72 X. G. Wan, A. M. Turner, A. Vishwanath and S. Y. Savrasov, *Phys. Rev. B*, 2011, **83**, 205101.
73 G. B. Halasz, L. Balents and , (2012). *Phys. Rev. B*, 2012, **85**.
74 M. Shuichi, *New J. Phys.*, 2007, **9**, 356-356.
75 Z. Wang, H. Weng, Q. Wu, X. Dai and Z. Fang, *Phys. Rev. B*, 2013, **88**, 125427.
76 K.-Y. Yang, Y.-M. Lu and Y. Ran, *Phys. Rev. B*, 2011, **84**, 075129.
77 M. Orlita, D. M. Basko, M. S. Zholudev, F. Teppe, W. Knap, V. I. Gavrilenko, N. N. Mikhailov, S. A. Dvoretskii, P. Neugebauer, C. Faugeras, A. L. Barra, G. Martinez and M. Potemski, *Nat. Phys.*, 2014, **10**, 233-238.
78 M. N. Chernodub, A. Cortijo, A. G. Grushin, K. Landsteiner and M. A. H. Vozediano, *Phys. Rev. B*, 2014, **89**, 89.
79 E. V. Gorbar, V. A. Miransky and I. A. Shovkovy, *Phys. Rev. B*, 2014, **89**, 085126.
80 Y. Ominato and M. Koshino, *Phys. Rev. B*, 2014, **89**, 054202.
81 X.-Q. Chen, R. H. Li, Y. Sun, X. Y. Cheng, D. Z. Li and Y. Y. Li, *arXiv:1408.0491*。, 2014.
82 J. Reynolds and C. Lane, *Phys. Rev.*, 1950, **79**, 405-406.
83 S. K. Kushwaha, J. W. Krizan, J. Xiong, T. Klimczuk, Q. D. Gibson, T. Liang, N. P. Ong and R. J. Cava, *J. Phys. Condens. Matter.*, 2014, **26**, 212201.
84 P. Hohenberg, *Phys. Rev. B*, 1964, **136**, 864.
85 W. Kohn and L. J. Sham, *Phys. Rev. A*, 1965, **140**, 1133.
86 G. Kresse and J. Hafner, *Phys. Rev. B*, 1993, **47**, 558-561.
87 G. Kresse and J. Furthmüller, *Comput. Mat. Sci.*, 1996, **6**, 15–50.
88 P. E. Blöchl, *Phys. Rev. B*, 1994, **49**, 16223-16233.
89 M. McMahon, R. Nelmes, U. Schwarz and K. Syassen, *Phys. Rev. B*, 2006, **74**, 140102.
90 M. I. McMahon, O. Degtyareva and R. J. Nelmes, *Phys. Rev. Lett.*, 2000, **85**, 4896-4899.
91 M. Mansmann, *Z. Kristallogr.,*, 1965, **122**, 399-406.
92 M. E. Leonova, I. K. Bdikin, S. A. Kulinich, O. K. Gulish, L. G. Sevast'yanova and K. P. Burdina, *Inorg. Mater.* , 2003, **39**, 266-270.
93 E. Zintl and W. Dullenkopf, *Z. Phys. Chem. B.*, 1932, **16**, 183-194.
94 J. P. Perdew, K. Burke and M. Ernzerhof, *Phys. Rev. Lett.*, 1996, **77**, 3865.
95 W. Tang, E. Sanville and G. Henkelman, *J. Phys. Condens. Matter.*, 2009, **21**, 084204.
96 A. Savin, R. Nesper, S. Wengert, & and T. F. Fässler, *Angew. Chem. Int. Ed. Engl.* , 1977, **36**, 1808-1832.
97 A. D. Becke and K. E. Edgecombe, *J. Chem. Phys.* , 1990, **92**, 5397.
98 B. Silvi and A. Savin, *Nature*, 1994, **371**, 683-686.
99 A. Togo, F. Oba and I. Tanaka, *Phys. Rev. B*, 2008, **78**, 134106.
100 K. Momma and F. Izumi, *J. Appl. Crystallogr.* , 2011, **44**, 1272-1276.
101 M. I. McMahon, E. Gregoryanz, L. F. Lundegaard, I. Loa, C. Guillaume, R. J. Nelmes, A. K. Kleppe, M. Amboage, H. Wilhelm and A. P. Jephcoat, *Proc. Natl. Acad. Sci. U. S. A.*, 2007, **104**, 17297-17299.
102 M. I. McMahon and R. J. Nelmes, *Chem. Soc. Rev.*, 2006, **35**, 943-963.
103 E. Gregoryanz, L. F. Lundegaard, M. I. McMahon, C. Guillaume, R. J. Nelmes and M. Mezouar, *Science*, 2008, **320**, 1054-1057.
104 A. Lazicki, A. F. Goncharov, V. V. Struzhkin, R. E. Cohen, Z. Liu, E. Gregoryanz, C. Guillaume, H. K. Mao and R. J. Hemley, *Proc. Natl. Acad. Sci. U. S. A.*, 2009, **106**, 6525-6528.
105 L. Lundegaard, M. Marqués, G. Stinton, G. Ackland, R. Nelmes and M. McMahon, *Phys. Rev. B*, 2009, **80**, 020101.
106 H. K. Mao, Y. Ding, Y. Xiao, P. Chow, J. Shu, S. Lebegue, A. Lazicki and R. Ahuja, *Proc. Natl. Acad. Sci. U. S. A.*, 2011, **108**, 20434-20437.
107 O. Degtyareva, M. I. McMahon and R. J. Nelmes, *High Pres. Res.*, 2004, **24**, 319-356.
108 W. Chaimayo, L. F. Lundegaard, I. Loa, G. W. Stinton, A. R. Lennie and M. I. McMahon, *High Pres. Res.*, 2012, **32**, 442-449.
109 D. A. Young, *Phase Diagrams of the Elements*, University of California Press, Berkeley 1991.
110 J. Sangster and A. D. Pelton, *J. Phase Equilib.*, 1991, **12**, 451-456.
111 P. Villars, ed., *Inorganic Solid Phases*, Springer & MPDS & NIMS, 2010.
112 G. Brauer and Z. E., *Z. Phys. Chem. Abstr.* , 1937, **37**, 323-352.
113 M. E. Leonova, S. A. Kulinich and L. G. Sevast'yanova, et al., *Exp. Geosci.*, 1998, **7**, 55-56.
114 S. A. Kulinich, M. E. Leonova and L. G. Sevast'yanova, et al. , *Zh. Obshch. Khim.*, 1999, **69**, 681-683.
115 B. A. Bernevig, T. L. Hughes and S. C. Zhang, *Science*, 2006, **314**, 1757-1761.
116 P. Giannozzi, S. Baroni, N. Bonini, M. Calandra, R. Car, C. Cavazzoni, D. Ceresoli, G. L. Chiarotti, M. Cococcioni, I. Dabo, A. Dal Corso, S. de Gironcoli, S. Fabris, G. Fratesi, R. Gebauer, U. Gerstmann, C. Gougoussis, A. Kokalj, M. Lazzeri, L. Martin-Samos, N. Marzari, F. Mauri, R. Mazzarello, S. Paolini, A. Pasquarello, L. Paulatto, C. Sbraccia, S. Scandolo, G. Sclauzero, A. P. Seitsonen, A. Smogunov, P. Umari and R. M. Wentzcovitch, *J. Phys. Condens. Matter.*, 2009, **21**, 395502.
117 P. B. Allen, *Phys. Rev. B*, 1975, **12**, 905-922.